# Experimental/Analytical Characterization of the RBCC Rocket-Ejector Mode

J. Ruf*, M. Lehman**, S. Pal**, R. J. Santoro** and J. West*

* NASA Marshall Space Flight Center
Applied Fluid Dynamics Analysis Group
Huntsville, AL 35812

** Penn State University
Department of Mechanical and Nuclear Engineering
The Pennsylvania State University
University Park, PA 16802

## ABSTRACT

Experimental and complementary CFD results from the study of the rocket-ejector mode of a Rocket Based Combined Cycle (RBCC) engine are presented and discussed. The experiments involved systematic flowfield measurements in a two-dimensional, variable geometry rocket-ejector system. The rocket-ejector system utilizes a single two-dimensional, gaseous oxygen/gaseous hydrogen rocket as the ejector. To gain a thorough understanding of the rocket-ejector's internal fluid mechanic/combustion phenomena, experiments were conducted with both direct-connect and sea-level static configurations for a range of rocket operating conditions. Overall system performance was obtained through global measurements of wall static pressure profiles, heat flux profiles and engine thrust, whereas detailed mixing and combustion information was obtained through Raman spectroscopy measurements of major species (oxygen, hydrogen, nitrogen and water vapor). The experimental results for both the direct-connect and sea-level static configurations are compared with CFD predictions of the flowfield.

## INTRODUCTION

Recent interest in low cost, reliable access to space has generated increased interest in advanced technology approaches to space transportation systems. A key to the success of such programs lies in the development of advanced propulsion systems capable of achieving the performance and operations goals required for the next generation of space vehicles. One extremely promising approach involves the combination of rocket and air-breathing engines into a rocket-based combined-cycle engine (RBCC). Although there are several design variations for the RBCC engine, the gamut of concepts includes four flight regimes, viz. rocket-ejector, ramjet, scramjet and all-rocket [1]. Of these four flight regimes, the rocket-ejector mode that encompasses vehicle flight Mach numbers from zero to roughly two is the least understood.

The present investigation utilizes an integrated experimental and computational fluid dynamics (CFD) approach to examine critical rocket-ejector performance issues. The experimental phase of this program, conducted at Penn State University, documents the mixing and combustion characteristics of the rocket-ejector system utilizing Raman spectroscopy in conjunction with heat flux, static pressure and thrust measurements. For this purpose, a two dimensional variable geometry rocket-ejector system with optical access was designed and fabricated. Complementary CFD analyses were conducted at NASA Marshall Space Flight Center to validate/refine the FDNS code [2] as well as to provide further insight into the rocket-ejector mode of operation.

To date, experiments have been conducted for both the Diffusion and Afterburning (DAB) as well as the Simultaneous Mixing and Combustion (SMC) rocket-ejector configurations [3-5]. In this paper, experimental and CFD results for only the DAB geometric configuration are presented and discussed. The experimental setup and CFD analysis methodology are introduced first before the experimental/analytical results are presented and discussed.

## EXPERIMENTAL

### EXPERIMENTAL SETUP AND RUN CONDITIONS

A single rocket based, optically accessible, air augmented rocket-ejector system was designed and fabricated for the experiments. The design of this two-dimensional configuration was based on the well-known 1968 experimental rocket-ejector study of Odegaard and Stroup [6]. The rocket was designed for gaseous hydrogen (GH₂)/gaseous oxygen (GO₂) propellants. Both direct-connect (forced air) and open inlets were available for the integrated rocket-ejector system. The maximum air, GO₂, and GH₂ flow rates of the facility are 5, 1, and 0.25 lbm/s, respectively.

The design of the air augmented rocket-ejector system stresses modularity for studying the important effects of nozzle primary area ratios, primary-secondary pressure matching and thermal choking. The complete air augmented

(a) Direct-connect configuration



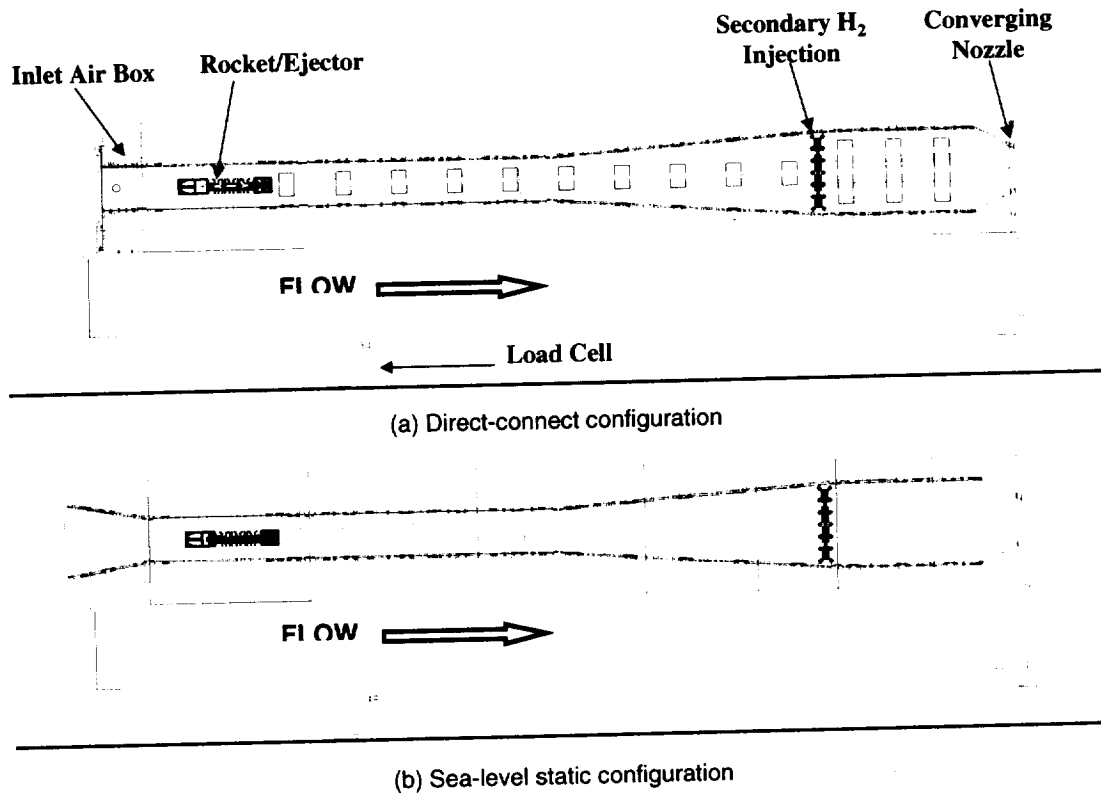(b) Sea-level static configuration

**Fig. 1.** Rocket-ejector setups.

rocket-ejector systems for the two configurations reported in this paper are shown in Fig. 1. The two-dimensional design enables convenient changes of the rocket-ejector's mixer length, diffuser length and angle, afterburner length and exit nozzle geometry. For the direct-connect DAB geometry shown at the top of Fig. 1, the mixer and diffuser length are both 35.0 in., whereas the internal width of the duct is 3.0 in. The internal height expands from 5.0 to 10 in. throughout the diffuser length, and the exit nozzle of the RBCC duct converges from 10.0 in. to an exit height of 5.0 in. For the complementary sea-level static DAB geometry shown in the bottom of Fig. 1, the direct-connect air box was replaced with a two-dimensional open inlet. The inlet height is 8.52 in. and reduces to 5.0 in. over a length of 10.0 in.

The single $GO_2/GH_2$ rocket-ejector was designed for optimum performance at an operational pressure of 500 psia at stoichiometric flow conditions. Six flow conditions have been investigated [3] and are defined in Table 1. In the present paper, experimental results and CFD predictions for only Cases 3 and 6 are presented. Experimental results for other cases can be found in Ref. 3. However, a brief description of all six cases is provided here. The flow conditions include both stoichiometric rocket/afterburner and fuel-rich rocket/no afterburner operation for a fixed rocket chamber pressure of 500 psia. In Table 1, for Case 1 and Case 2, the operating mixture ratio of the rocket was four. The two cases differ in the amount of air introduced into the system. For Case 1, the excess $GH_2$ in the rocket plume depletes the $GO_2$ in the air stream, whereas for Case 2, the airflow is defined such that the $GO_2$ in the air can burn stoichiometrically (O/F=8) with the excess $GH_2$ in the rocket exhaust. For these two cases, there is no downstream introduction of $GH_2$. For Cases 3 and 4, the operating $GO_2/GH_2$ mixture ratio was stoichiometric. The two conditions differ in the amount of air introduced, and therefore in the bypass ratio studied, which is defined as the ratio between the airflow and total propellant flow. For these two cases, the afterburner was operational and the amount of $GH_2$ injected was set to achieve stoichiometric burning with the $GO_2$ in the air stream. The inlet geometry of the ejector used direct-connect for simulating conditions of Mach 1 at 9400 ft and Mach 1.9 at 40,000 ft for a nominal 1000 psf dynamic pressure trajectory. These conditions are the same as those tested for the Odegaard and Stroup study [6]. The sea-level static tests, viz. Cases 5 and 6, used identical rocket flow rates as Case 1 and Case 3, but the air flow rate was measured using a differential pressure gauge to quantify the amount of air ejected through the engine under typical operating conditions.

The compact rectangular cross-sectioned gaseous hydrogen/oxygen rocket was designed specifically to integrate into the rocket-ejector assembly (Fig. 2). The rocket injector body utilizes 6 shear coaxial elements in a horizontal array and is not actively cooled. The internal dimensions of the chamber section are 6.6 in. long, 3.0 in.

<div align="center">**Table 1.*** Summary of flow conditions.</div>

| | Direct-connect | | | | Sea-level Static | |
| --- | --- | --- | --- | --- | --- | --- |
| | Case 1 | Case 2 | Case 3 | Case 4 | Case 5 | Case 6 |
| **Rocket** | | | | | | |
| O/F | 4 | 4 | 8 | 8 | 4 | 8 |
| $GO_2$ Flowrate (lbm/s) | 0.470 | 0.470 | 0.608 | 0.608 | 0.470 | 0.608 |
| $GH_2$ Flowrate (lbm/s) | 0.118 | 0.118 | 0.076 | 0.076 | 0.118 | 0.076 |
| Chamber Pressure (psia) | 500 | 500 | 500 | 500 | 500 | 500 |
| **Duct** | | | | | | |
| Air Flow (lbm/s) | 1.575 | 2.016 | 1.575 | 2.016 | *1.29*** | *1.24*** |
| Bypass Ratio | 2.68 | 3.43 | 2.30 | 2.95 | *2.19* | *1.81* |
| $GH_2$ Flow in Afterburner (lbm/s) | 0 | 0 | 0.046 | 0.059 | 0 | 0.046 |
| Excess $GH_2$ in Rocket Exhaust (lbm/s) | 0.059 | 0.059 | 0 | 0 | 0.059 | 0 |
| $GO_2$ in Airflow (lbm/s) | 0.368 | 0.470 | 0.368 | 0.470 | *0.301* | *0.290* |
| O/F Between $GO_2$ in Air and $GH_2$ in Duct | 6.25 | 8 | 8 | 8 | *5.02* | *6.30* |

* Results for only Cases 3 and 6 (shaded) are discussed in this paper.
** For sea-level static conditions, ejected airflow rate is measured. Items in *italics* were calculated after experiments.

wide and 0.5 in. tall. The nozzle reduces to a throat height of 0.1 in. and expands to a height of 0.6 in. The rocket chamber and converging/diverging nozzle sections are both actively cooled with water during each firing.

The RBCC duct also features multiple locations for optical access to the flow. Window ports for quartz windows are present on all four walls and allow both camera visualization and laser transmission. The first window is centered 2.5 in. from the rocket/ejector exit plane. Each subsequent window is spaced 7.0 in. farther downstream. The side wall windows measure 2.0 × 3.0 in. The top window locations were used only for laser transmission into the RBCC duct for Raman spectroscopy species measurements (discussed later). As designed, the top window location was too near the focal point of the laser beam being passed into the RBCC duct, and breakdown of the quartz material resulted. The 1.0 × 2.0 in. top window was replaced with a copper blank that had been modified to accept a 18.0 in. long, 0.5 in. diameter extension tube. The bottom of the tube was silver soldered to a straight hole in the blank, and the top was fitted with a 2.0 in. diameter quartz window purged with helium. The corresponding bottom window location was fitted with a beam dump for collection of the transmitted laser beam.

## DIAGNOSTICS

The entire RBCC system is mounted on a load cell for thrust measurements and is equipped with multiple static pressure ports and heat flux gauges along the vertical and horizontal duct walls. The load cell has a full-scale range of 1000 lbf. and is sampled at 200 Hz. The static pressure system uses 16 pressure taps on both the side and top walls of the RBCC duct. Each pressure tap has an individual transducer, and is sampled at 6 Hz. The pressure taps are equipped with a $N_2$ purge to clear condensation between runs. Eight Gardon type heat flux gauges were used to acquire data at 200 Hz. Between runs, these gauges were moved among locations on the side and top wall of the RBCC duct.

The primary diagnostic technique employed for documenting the mixing/combustion characteristics between the rocket exhaust and the airflow was Raman spectroscopy. For the present experiments, the technique was implemented for line measurements of the major species, viz. $GH_2$, $GO_2$, gaseous nitrogen ($GN_2$) and water vapor ($H_2O$). The setup schematic is shown in Fig. 3. A frequency doubled Nd:YAG laser, $\lambda = 532$ nm, was used as the excitation source. The laser beam was passed vertically through the RBCC duct in a focused line. The laser operated at a short pulse length of approximately 12 ns and produced 750 mJ per pulse. This resulted in an energy flux that exceeded the damage threshold of the quartz windows used to transmit the beam through the RBCC duct. To overcome this limitation, the laser pulse was stretched by means of a beam splitter and pulse delay path length.
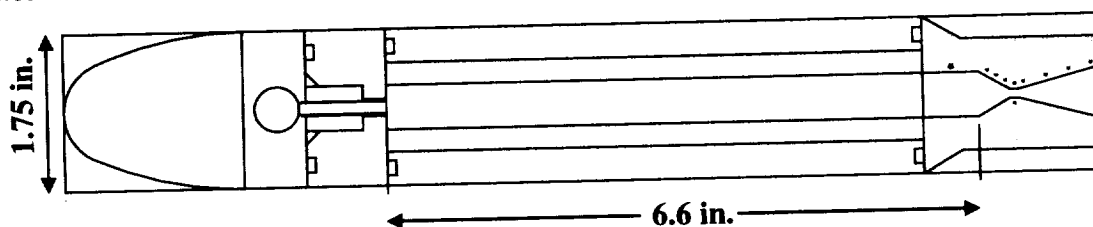


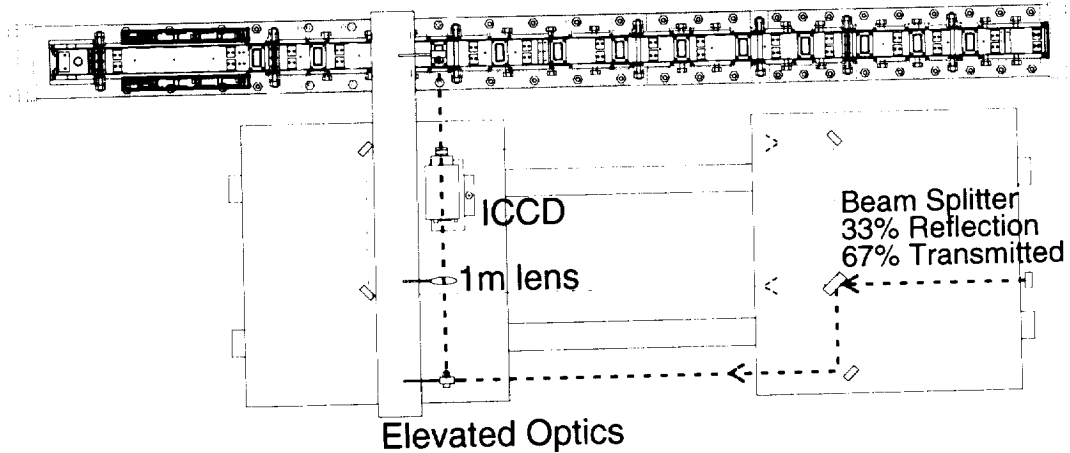**Fig. 2.** Schematic of two-dimensional gaseous oxygen/gaseous hydrogen rocket chamber.

**Fig. 3.** Top view of Raman spectroscopy setup.

This served to stretch the pulse to nearly 30 ns. After the beam had traveled along the pulse delay path, the laser beam was then directed vertically up to an elevated optical rail that redirected the beam over the top of the RBCC duct. After the beam passed through a 1 m focusing lens, it was reflected down through the RBCC duct by means of the previously mentioned sealed quartz window. The focal point of the laser beam matched the centerline of the RBCC duct and the side window. Through this window, the Raman signal was collected at 90° to the beam by an ICCD camera (12 bit dynamic range; EEV CCD chip, 576 × 384 pixels) using either an imaging spectrometer or species specific bandpass filters with a f/1.2 50 mm fl Nikon lens. The spectrometer was used only at the first window location, 2.5 inches downstream from the rocket nozzle exit plane, and required 4x6 pixel binning for image analysis. Beyond the first window, species specific 10 nm bandpass filters were required due to their higher signal collection efficiency, and 4 × 4 pixel binning was used. For the wavelength of the laser used here ($\lambda$ = 532 nm), the peak wavelengths for the Stokes vibrational Q-branch Raman signals from $GO_2$, $GH_2$, $GN_2$ and $H_2O$ are 580, 680, 607 and 660 nm, respectively [7-9]. For each firing, the collected Raman signal was then sent to a personal computer for data storage and eventual analysis. The laser operated at 10 Hz, but the camera readout rate slowed acquisition to approximately 5 Hz. The test duration was set for 4 seconds of steady state combustion. Using this timing sequence, each firing provided 15-20 instantaneous Raman images. Images were then discarded or retained based on image quality. Images that had pixel saturation in any region were not included in the averaging process. The technique was applied for making species measurements at the first four window locations downstream of the rocket nozzle exit plane. The goal was to establish at what location the flow of the ejector was fully mixed with the air and at what location any excess $GH_2$ had been consumed. This provides key information on the mixing and combustion characteristics that can then be applied for improving numerical models being developed.

The analysis procedure for calculating the major species' concentration profiles and temperature from the Raman signal measurements is briefly described. Eq. 1 shows how the Raman signal intensity relates to the individual species mole fractions and the overall gas temperature and pressure.

$$S_i = k_i f_i(T)\eta_i \tag{1}$$

$S_i$ = Raman Signal Intensity
$k_i$ = Signal Collection Constant
$f_i(T)$ = Bandwidth Factor
$\eta_i$ = Species Number Density
In terms of species' mole fraction,

$$\chi_i = \frac{S_i}{f_i(T)k_i\left(\frac{P}{RT}\right)} \tag{2}$$

where P, T and R are the pressure, temperature and gas constant, respectively.

The signal collection constant, $k_i$, is obtained from cold flow of pure species through the rocket body. With temperature and pressure equal to ambient conditions, Raman signal was collected, mole fraction and $f_i(T)$ were set to unity, and so then the sole unknown in Eq. 1 was $k_i$. This signal collection constant was then applied to the hot fire analysis. For hot fire conditions, the Raman signal was again collected, but mole fraction, bandwidth factors and temperature of the species were not known. The bandwidth factor term accounts for variation in the fraction of total

4

scattered signal. It depends on spectral location, line shape, and bandwidth of the detection system. The $f_i(T)$ term was expressed in the form of a polynomial curve fit theoretically determined [10] for the range of temperatures expected in these experiments, 300K-3500K. The final analysis then required iteration based on temperature. The temperature was varied until the sum of the mole fractions for the four species ($H_2$, $O_2$, $H_2O$ and $N_2$) was unity, using Eq. 1 and the four bandwidth factor polynomials. This iteration was done for each of the vertical pixel locations in the Raman signal field of view in order to return corresponding temperature and mole fraction profiles within the duct.

# COMPUTATIONAL

## SOLUTION ALGORITHM

FDNS is a general purpose, multidimensional, multi-species, viscous flow, pressure-based reacting flow solver. FDNS solves the Reynolds-averaged transport equations with a variety of options for physical models and boundary conditions. To solve the system of nonlinear partial differential equations, the code uses finite-difference approximations to establish a system of linearized algebraic equations. Several difference schemes were employed to approximate the convective terms of the momentum, energy and continuity equations, including central difference [2], upwind and total-variation-diminishing (TVD) schemes [11]. Viscous fluxes and source terms are discretized using a central-difference approximation. A pressure-based predictor plus multiple-corrector solution method is employed so that flow over a wide speed range (from low subsonic to supersonic) can be analyzed

Both standard and extended two-equation turbulence model [12] closure can be used to describe the turbulent flow. The compressibility effect on the turbulence is taken into account by the method of Mach-number correction. A modified wall function approach [13] is employed by incorporating a complete velocity profile [14]. This complete velocity profile provides a smooth transition between Logarithmic law-of-the-wall and linear viscous sublayer velocity distributions. Details of the present numerical methodology are given by Ref 2.

Both the direct-connect and sea-level static simulations were solved steady state, implementing the third order TVD scheme. The direct-connect case used an extended two-equation turbulence model with the compressibility correction. The sea-level static case used the standard two-equation turbulence model with compressibility correction. Both the direct-connect and sea-level static solutions solved the GO2/GH2 combustion physics finite rate with a system of seven species and nine reactions [15].

## GRID AND BOUNDARY CONDITIONS

The computational domains consisted of one quarter of the experimental hardware internal flow path. Symmetry planes were used on the vertical and horizontal centerlines. Structured grids were implemented. The direct-connect grid contained 570,000 nodes in 12 zones and the sea-level static grid contained 510,000 nodes in 13 zones. Non-matching zonal boundaries were implemented at several locations to keep the number of nodes from becoming excessive.

The direct-connect and sea-level static computational domains differed in the forward end of the RBCC. The direct-connect forward end was closed off and had air supplied to it. The computational domain included one half of each of two of the circular air supply orifices, modeled as equivalent area square orifices. A subsonic fixed mass flow boundary was applied to the air supply orifices. The flow straighteners downstream of the air inlets were not modeled. The sea-level static domain forward end was open to ambient air. The entrained air flow rate was not specified, but solved for. The zones upstream of the inlet had far-field freestream boundary conditions specified on their perimeter. Flow straighteners were not used in the test hardware so none were modeled.

From the rocket nozzle exit through the remainder of the domains the grids and boundary conditions were similar. The rocket engine internal flow computation was performed in another effort [16]. One quarter of the rocket engine's exit plane was discretized in the domains. The rocket nozzle exit was set as a fixed inlet boundary condition. The rocket flow was three-dimensional with an average Mach number of approximately 2.6 and static pressure of one atmosphere. In both domains the afterburner injection ports were modeled as equivalent area square orifices with a fixed inlet flow of Mach 1.3. The rocket engine, air, and afterburner flow rates are shown in Table 1. The physical walls of the hardware were set as no-slip boundaries and the symmetry planes were specified as such. Both domains contain a freestream region downstream of the RBCC nozzle with a far-field boundary condition applied to the perimeter. The right-most face of the domains was set as an exit boundary.
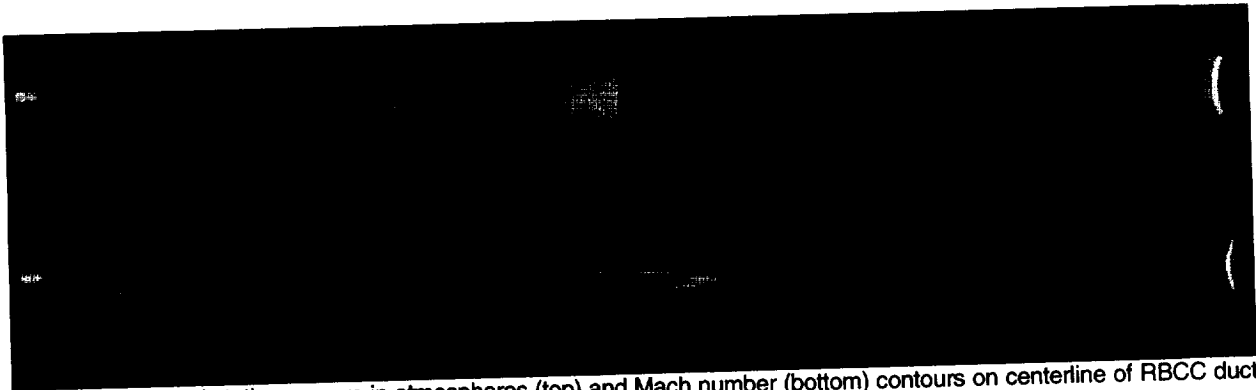
**Fig. 4.** Calculated static pressure in atmospheres (top) and Mach number (bottom) contours on centerline of RBCC duct for direct-connect configuration, Case 3 (see Table 1).

## RESULTS AND DISCUSSION

Results are presented and discussed for the direct-connect, Case 3, and sea-level static, Case 6, in the following order; flow field overview, major specie mole fractions, entrained air flow (Case 6 only), static pressures and thrust and specific impulse. Experimental and computational results are presented simultaneously for all but the flow field overview.

### FLOW FIELD OVERVIEW

Static pressure (in atmospheres) and Mach number distributions from the CFD analysis are shown as color contours in Figs. 4 and 5 for the direct-connect and sea-level static configurations, respectively. In both figures, only a portion of the freestream zones is displayed. The forward end of the two cases are clearly different. The effect of the introduced direct-connect air flow is visible on the left hand side of Fig. 4, whereas the entrained air in Fig. 5 is seen as relatively low speed and uniform.

The rocket engine plumes are clearly visible in the middle of the RBCC ducts. For both cases the flow was generally two-dimensional between the rocket engine exit and afterburner hydrogen injection (the mixer and diffuser sections.) Note the axial stations at which the pressure began to rise in the mixer sections were coincident with the rocket engine plumes attachment to the upper (and lower) walls. Close observation of the rocket plumes show that the direct-connect's rocket plume did not expand as much as the sea-level static's rocket plume. This was caused by the slightly higher pressures in the forward half of the direct-connect mixing section.

In both case's the Mach number contours indicate the flow was entirely subsonic as it entered the diffuser section of the duct. The effect of the afterburner hydrogen injection is visible at the end of the diffuser. In neither case did the flow choke at the RBCC throat. The average nozzle exit Mach numbers were approximately 0.85 and 0.78 for the direct-connect and sea-level static cases, respectively.

### MAJOR SPECIES MOLE FRACTIONS

Experimental and computational results of major species concentrations are presented for direct-connect and sea-level static cases in Figs. 6 and 7, respectively. For both these cases, the rocket was operated stoichiometrically
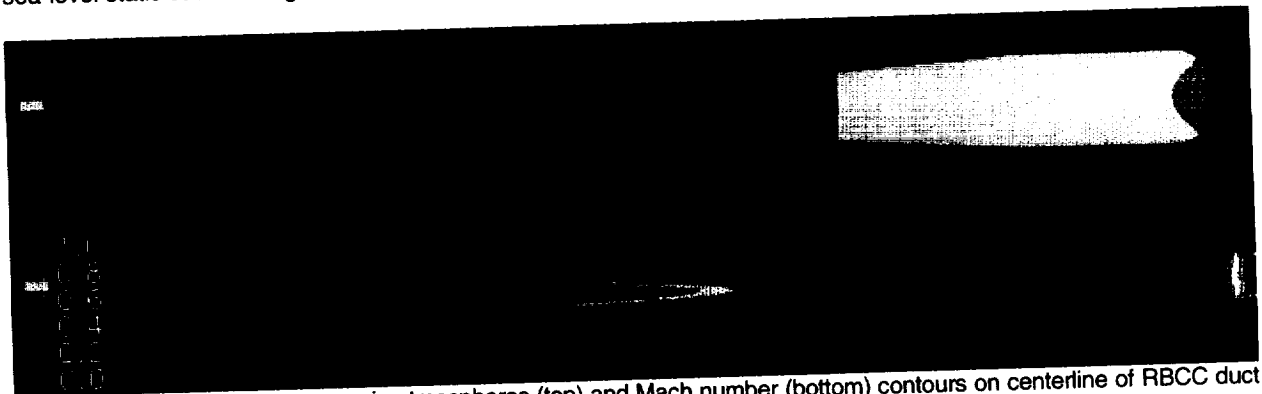


**Fig. 5.** Calculated static pressure in atmospheres (top) and Mach number (bottom) contours on centerline of RBCC duct for sea-level static configuration, Case 6 (see Table 1).
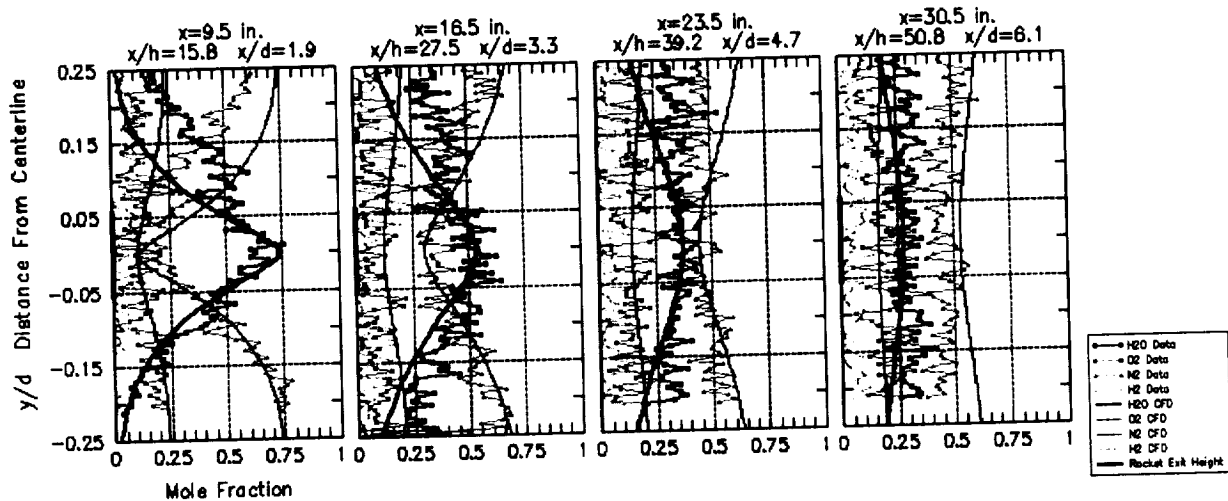
**Fig. 6.** Mole fraction comparison for direct connect configuration, Case 3 (see Table 1).

at a target chamber pressure of 500 psia (see Table 1). In these figures the flow was from left to right. The experimental data (the lines with symbols) will be discussed first. In Fig. 6 results are shown for the second through fifth window locations and in Fig. 7 results are shown for the second, third and fourth window locations. From Fig. 6, inspection of the direct-connect species profiles shows that the profiles were nearly uniform at the fourth measurement location (x=23.5 in.) and were uniform at the fifth measurement location (x=30.5 in.) For the sea-level static results, the species profiles approached a uniform distribution by the third measurement location (x=16.5 in.), and the flow was homogeneous at the fourth measurement location (x=23.5 in.) This significant variation in the measured mixing length was the result of two related phenomena; different air flow rates and plume expansion angles. As indicated in Table 1 the direct-connect case had air introduced at a rate of 1.575 lbm/s, whereas the sea-level static case ejected air at 1.24 lbm/s. The larger air flow rate in the direct-connect case required additional mixing length for the plume to mix completely with the air. Also, as discussed above, the direct-connect rocket plume expansion angle was slightly lower than the sea-level static rocket plume. The lower plume expansion angle resulted in slower convective mixing with the air. The combined effect of these two phenomena was that the direct-connect case required a mixing length about seven inches longer than the sea-level static case.

The computed specie concentrations are shown as solid lines in Figs. 6 and 7. The computed direct-connect concentrations matched the data fairly well at the second, third and fourth measurement locations. At the fifth measurement location the computed concentrations were not completely mixed out. The computed specie concentrations for the sea-level static case (Fig. 7) matched the test data fairly well at the second and third measurement locations. Again the computed concentrations at the last measurement location were not completely mixed out.
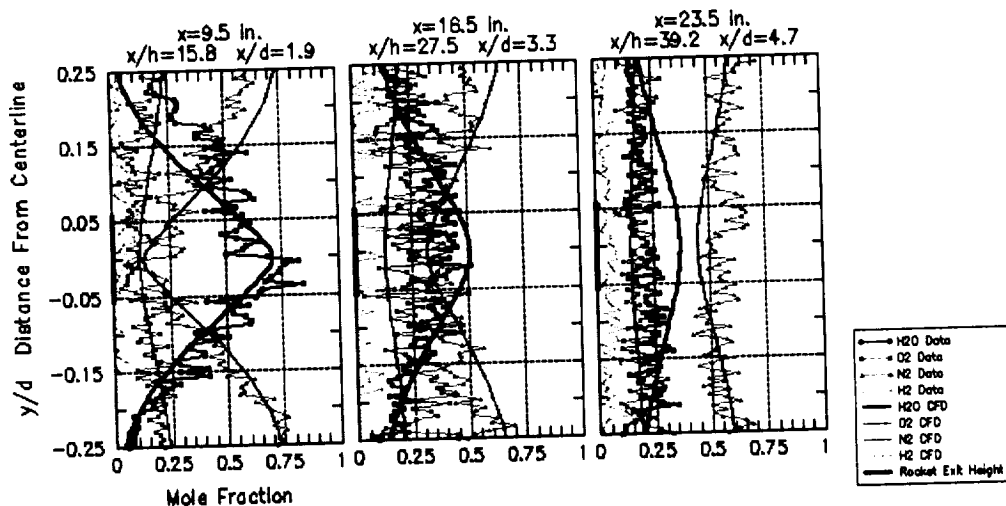


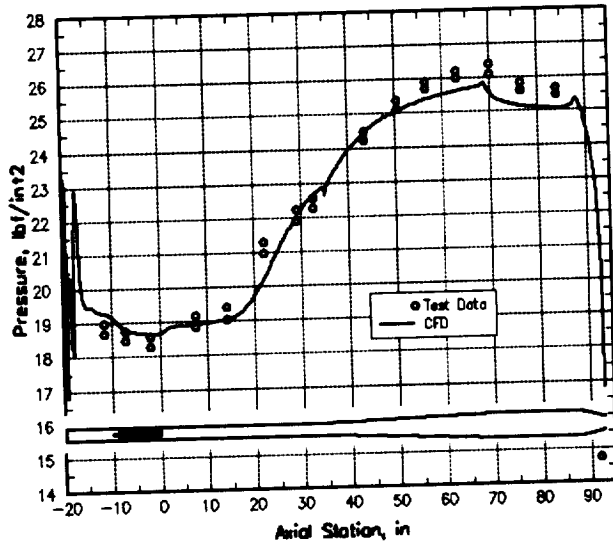**Fig. 7.** Mole fraction comparison for sea-level static configuration, Case 6 (see Table 1).

7

**Fig. 8.** Static pressure comparison for direct connect configuration, Case 3 (see Table 1).
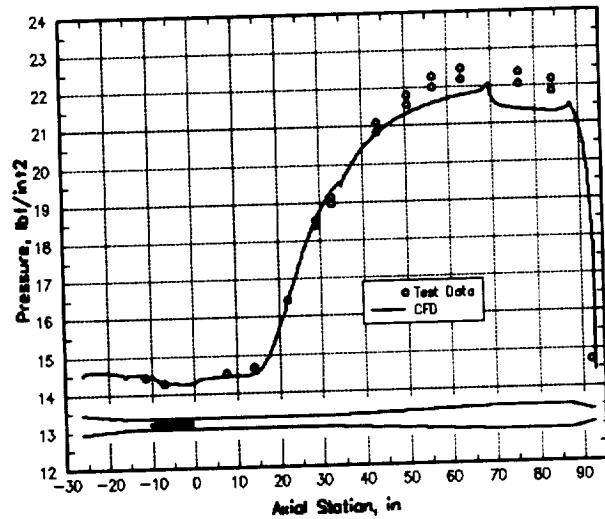


**Fig. 9.** Static pressure comparison for sea-level static configuration, Case 6 (see Table 1).

**Table 2.** Thrust and $I_{sp}$.

| | | Experiment | Computation | % Error |
|---|---|---|---|---|
| **Case 3** | Thrust (lbf) | 266.6 | 260.3 | 2.4 |
| **Direct-Connect** | $I_{sp}$ (s$^{-1}$) | 366.6 | 357.4 | 2.5 |
| **Case 6** | Thrust (lbf) | 200.1 | 174.0 | 13.0 |
| **Sea-Level Static** | $I_{sp}$ (s$^{-1}$) | 275.8 | 238.6 | 13.5 |

## ENTRAINED AIR

The experimental data for sea-level static, Case 6, indicated a by-pass ratio (mass flow of air/mass flow of rocket) of 1.84. The computed by-pass ratio was 1.51, or 18% below the test data. The source of the error in the computation is as of yet unexplained.

## STATIC PRESSURES

The static pressure results for the direct-connect and sea-level static cases are presented in Figs. 8 and 9, respectively. The experimental data shown in both figures were two individual tests with nominal flow rates for the air, rocket engine and afterburner. The difference in pressures at each point between the two tests is representative of the test-to-test variation. For each case, side and top wall experimental measurements were identical. Note that the higher air flow rate of the direct-connect case increased the static pressure throughout the entire RBCC duct. Both cases show a sharp rise in pressure at about the same axial location that the specie concentrations indicated significant mixing had occurred. The rise in pressure continued through the diffuser up to the injection of the afterburner fuel. The pressure dropped slightly due to the heat addition and subsequent acceleration of the flow. The pressure was relatively flat in the constant area afterburner and then dropped rapidly as the flow accelerated out the nozzle

The computed pressures generally agreed well with the test data. The spikes in the left hand side of Fig. 8 were caused by the direct-connect air inlets. In both cases the computed pressure began to rise at the same location as the measured pressures. The rate of increase of the computed pressure rise was slightly below that of the measured pressures. Therefore, the computed pressure in the afterburner sections were 2.0 and 4.5 percent low for the direct-connect and sea-level static cases respectively.

## THRUST AND SPECIFIC IMPULSE

The experimental and computational values for thrust and specific impulse ($I_{sp}$) are presented in Table 2. The experimental values were averaged for the two test points use for each case in the static pressure plots. For the direct-connect case the 2.4 and 2.5 percent errors in computed thrust and $I_{sp}$ resulted from the two percent low

pressure in the afterburner. The larger errors in the computed thrust and $I_{sp}$ for the sea-level static case were largely a result of the combined effect of the low air entrainment and low afterburner pressure.

## SUMMARY

Raman spectroscopy was applied to study the mixing and combustion characteristics between the rocket exhaust plume and the air stream in an optically-accessible hydrogen/oxygen rocket-ejector system. Experiments were conducted for both direct-connect and SLS configurations for a fixed rocket chamber of 500 psia. Computational fluid dynamics analysis was performed for two specific test cases. The results of the CFD analysis compared favorably with the test data.

## ACKNOWLEDGEMENTS

## REFERENCES

[1] Escher, W. J. D., ed., The Synerjet Engine: Airbreathing/Rocket Combined-Cycle Propulsion for Tomorrow's Space Transports, Society of Automotive Engineers, Warrendale, PA, 1997.

[2] Wang, T.-S. and Chen, Y.-S., "Unified Navier-Stokes Flowfield and Performance Analysis of Liquid Rocket Engines," Journal of Propulsion and Power, Vol. 9, No. 5, Sept-Oct 1993, pp.678-685.

[3] Lehman, M., Pal, S. and Santoro, R. J., "Experimental Investigation of the RBCC Rocket-Ejector Mode," AIAA 2000-3725, 36th Joint Propulsion Conference, Huntsville, AL, July 17-19, 2000.

[4] Lehman, M., Pal, S., Broda, J. C. and Santoro, R. J., "Raman Spectroscopy Based Studies of RBCC Ejector Mode Performance," AIAA-99-0090, 37th AIAA Aerospace Sciences Meeting, Reno, NV, January 11-14, 1999.

[5] Lehman, M., Pal, S. and Santoro, R. J., "Experimental Studies of the RBCC Rocket-Ejector Mode," Joint Meeting of the United States Sections: The Combustion Institute, Washington, DC, March 15-17, 1999.

[6] Odegaard, E. A. and Stroup, K. E., "1966 Advanced Ramjet Concepts program, Volume VIII-Ejector Ramjet Engine Tests- Phase I" The Marquardt Corporation, Technical Report AFAPL-TR-67-118 Volume VIII, January 1968.

[7] Herzberg, G., Molecular Spectra and Molecular Structure, Vol. I - Spectra of Diatomic Molecules, Van Nostrand Reinhold Company, Krieger Publishing Company, 1950, Reprinted 1989.

[8] Herzberg, G., Molecular Spectra and Molecular Structure, Vol. II - Infrared and Raman Spectra of Polyatomic Molecules, Van Nostrand Reinhold Company, Krieger Publishing Company, 1945, Reprinted 1991.

[9] Herzberg, G. and Huber, K.P., Molecular Spectra and Molecular Structure, Vol. IV - Constants of Diatomic Molecules, Van Nostrand Reinhold Company, Krieger Publishing Company, 1979.

[10] Hassel, E. P., Raman Scattering Experiment Simulator (RAMSES) Version 2.0. Institute fur Energie- und Fraftwerkstechnik, Technische Hochschule, Darmstadt, Germany, 1996.

[11] Chen, Y.-S., Liaw, P., Shang, H.-M. and Chen, C. P., "Numerical Analysis of Complex Internal and External Viscous Flows with a Second-Order Pressure-Based Method," AIAA Paper 93-2966, July 1993.

[12] Chen, Y.-S. and Kim S. W., "Computation of Turbulent Flows Using an Extended $\kappa$-$\epsilon$ Turbulence Closure Model," NASA CR-179204, Oct. 1987.

[13] Chen, Y.-S., Cheng, G. C. and Farmer, R. C., "Reacting and Non-Reacting Flow Simulation for Film Cooling in 2-D Supersonic Flows," AIAA Paper 92-3602, July 1992.

[14] Liakopouls, A., "Explicit Representations of the Complete Velocity Profile in a Turbulent Boundary Layer," AIAA Journal, Vol. 22, No. 6, Jan. 1984, pp. 844-846.

[15] Wang, T.-S., McConnaughey, P., Warsi, S., and Chen, Y.-S., "Computational Pollutant Environment Assessment from Propulsion System Testing," Journal of Spacecraft and Rockets, Vol. 33, No. 3, May-June 1996, pp.386-392.

[16] Pal, S., Tucker, T., Lehman, M., and Santoro, R., J., "Experimental Studies of Heat Transfer in Rectangular Nozzles for CFD Design Methodology" Paper NHTC99-252, 33rd ASME/AIChE/ANS/AIAA National Heat Transfer Conference, August 1999.